



OPEN

SUBJECT AREAS:

COMPUTATIONAL
BIOPHYSICS

MECHANISM OF ACTION

BIOLOGICAL PHYSICS

SUPRAMOLECULAR ASSEMBLY

α -Helical Structures Drive Early Stages of Self-Assembly of Amyloidogenic Amyloid Polypeptide Aggregate Formation in Membranes

Martina Pannuzzo¹, Antonio Raudino², Danilo Milardi³, Carmelo La Rosa² & Mikko Karttunen⁴

Received

21 May 2013

Accepted

3 September 2013

Published

27 September 2013

Correspondence and requests for materials should be addressed to C.L.R. (clarosa@unict.it) or M.K. (mikko.karttunen@uwaterloo.ca)

¹Department of Computational Biology, University of Erlangen-Nuremberg, Staudtstr. 5, 91058 Erlangen, Germany, ²Department of Chemical Sciences, University of Catania, Viale Andrea Doria 6, Catania, Italy I-95125, ³Istituto di Biostrutture e Bioimmagini, CNR, Unità Organizzativa e di Supporto di Catania, Viale A. Doria 6, Catania, Italy I-95125, ⁴Department of Chemistry & Waterloo Institute for Nanotechnology, University of Waterloo, 200 University Avenue West, Waterloo, Ontario, Canada N2L 3G1.

The human islet amyloid polypeptide (hIAPP) is the primary component in the toxic islet amyloid deposits in type-2 diabetes. hIAPP self-assembles to aggregates that permeabilize membranes and constitutes amyloid plaques. Uncovering the mechanisms of amyloid self-assembly is the key to understanding amyloid toxicity and treatment. Although structurally similar, hIAPP's rat counterpart, the rat islet amyloid polypeptide (rIAPP), is non-toxic. It has been a puzzle why these peptides behave so differently. We combined multiscale modelling and theory to explain the drastically different dynamics of hIAPP and rIAPP: The differences stem from electrostatic dipolar interactions. hIAPP forms pentameric aggregates with the hydrophobic residues facing the membrane core and stabilizing water-conducting pores. We give predictions for pore sizes, the number of hIAPP peptides, and aggregate morphology. We show the importance of curvature-induced stress at the early stages of hIAPP assembly and the α -helical structures over β -sheets. This agrees with recent fluorescence spectroscopy experiments.

Amyloidoses are a class of diseases including Type II Diabetes Mellitus, Alzheimer's and Parkinson's. These diseases are characterized by the conversion of peptides or proteins from their soluble functional states into fibrillar aggregates¹. The formation and buildup of these dense amyloid plaques has been widely accepted as the primary cause of disease (amyloid hypothesis)².

The amyloid hypothesis is challenged by the observation that a large number of Alzheimer's patients³ with amyloid plaques in the brain show no symptoms⁴⁻⁷. Similarly, amyloid deposition in type II diabetes is evident in only about 90% of patients^{8,9} and the remaining 10% do not develop any significant amyloid deposition¹⁰. This evidence substantiates the hypothesis that soluble, small-sized oligomers rather than mature fibrils may be the root of the pathogenic state. Thus, understanding the early steps of their formation, oligomeric interactions, and inhibition are among the key issues and prerequisites to develop effective therapies¹¹⁻¹³. In general, the mechanism(s) by which amyloid intermediates cause cytotoxicity and disease remains unresolved. Nevertheless, the inhibition of amyloid toxicity by a common antibody, independent of the location of the oligomers in extracellular or intracellular compartments, clearly supports a common mechanism in areas which are accessible via extra- and intracellular regions, such as cell membranes¹⁴⁻¹⁸.

In general, amyloid-forming peptides are amphipathic. They may cause membrane perturbation through changes in bilayer fluidity, generate protein-stabilized pores (poration), lay on one leaflet of the membrane (carpeting), or remove lipid components from the bilayer by a detergent-like mechanism¹⁹. A recent study has also suggested a two-step mechanism for amyloid β induced disruption and pore formation with properties such as ion selectivity²⁰. There is, however, no consensus regarding which membrane perturbations are the most relevant to disease²¹. It has also been shown that the formation of amyloid fibers is a separate process from membrane disruption²² and that the composition of membrane and ions may have a significant influence on membrane disruption²³. Brender et al.²⁴ provide an excellent review of membrane disruption induced by IAPP.

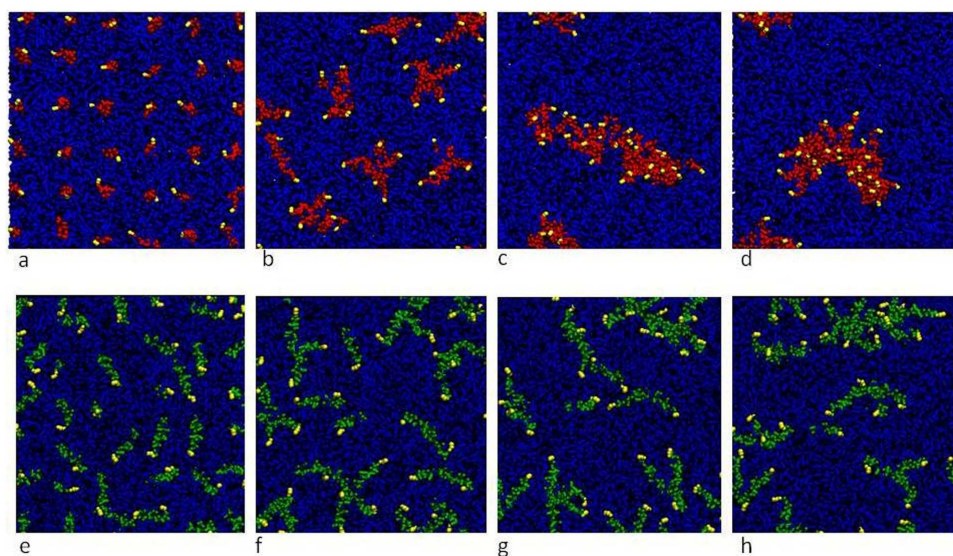


Figure 1 | Self-assembly of membrane-embedded hIAPP or rIAPP give rise to differently structured peptide aggregates. Top view from a simulation of peptide aggregation at 300 K for hIAPP (red) and rIAPP (green). Snapshots were taken at 1.0 μ s (a,e), 7.0 μ s (b,f), 13.0 μ s (c,g), 20.0 μ s (d,h) respectively. Lipids: blue. Yellow shows the lysine residues.

Islet Amyloid Polypeptide (IAPP) is the primary component in the pancreatic islet amyloid deposits observed in type 2 diabetes^{25,26}. Human IAPP (hIAPP) is a 37 amino acid peptide produced in the islet β -cells and co-secreted with insulin. Like other amyloid-forming peptides, hIAPP has been observed permeabilizing lipid membranes^{27–31}. The toxic oligomeric state of IAPP and its interaction with membranes has recently gained attention^{4,32,33}, but its transient nature makes experimental characterization highly elusive³⁴. It is known that addition of IAPP results in unspecific pore formation in membrane conductance experiments³⁵. Yet, some studies point to the critical role of hIAPP monomers in membrane interactions^{36,37}. Whether monomers, dimers or some larger structure are the most important in triggering membrane damage remains to be established.

Molecular dynamics (MD) is the only available technique for obtaining protein data at atomistic spatial resolution and microsecond, or finer, temporal resolution. MD simulations provide an invaluable tool to study the early steps of membrane-bound IAPP oligomerization and its effect on membrane integrity. There are several *in silico* studies of IAPPs, but, thus far the most extensive ones have focused on the free state structure in solution^{38–40}. All Atom (AA) and Coarse Grained (CG) MD studies of IAPP in membrane^{41,42} addressing the conformational equilibria of IAPP monomeric state have been also reported⁴³. In these studies, the β -strand conformation was assumed as the initial state³⁴. None of these studies, however, could single out the IAPP oligomers population and the variation of the membrane structure during self-assembly. To address this, we chose a different approach and performed a multiscale modeling study of the self-assembly and oligomerization of monomeric α -helical IAPP peptides in a model lipid bilayer (palmitoyl-oleyl-phosphatidylcholine (POPC) in a microsecond time scale. We employed a combination of atomistic MD (to explore the conformation of the assembled proteins) and CG simulations (to unveil the dynamics of protein aggregation in membrane) and used a mapping procedure to switch between the different levels of representations. Based on the outcome of simulations, we developed a thermodynamic model for aggregate formation. By combining the computational and analytical approaches, we demonstrate and explain the drastically different dynamics of oligomerization of hIAPP and its non-amyloidogenic rat variant (rIAPP). Our results underscore the importance of electrostatic dipolar interactions for

determining the shape of membrane-bound hIAPP aggregates as well as their impact on membrane physical properties.

Results

Self-assembly of hIAPP in a POPC lipid bilayer. We start by comparing the CG simulations of 36 hIAPP and as control 36 rIAPP peptides in α -helix conformations (26 μ s at 300 K) in a POPC membrane at 1:44 peptide-lipid molar ratio (Fig. 1). This ratio and secondary structure were chosen in order to simulate typical experimental conditions^{44,36}. All hIAPP peptides remained fully inserted in the membrane spanning from one leaflet to the other. They diffused laterally and self-assembled to form aggregates.

Short time behavior. Dimers, trimers and tetramers started to form within the first 10 ns. At ~ 6 μ s, dimers and trimers had virtually disappeared and only clusters made of 4–6 peptides were present. Once formed, these clusters diffused as a single unit and peptides did not dissociate from them. Repeated simulations at different protein concentrations exhibit a size concentration dependence behavior.

Longer time behavior. Larger aggregates started to form at ~ 12 μ s and after ~ 20 μ s (protein/lipid ratio of 1:44), a large, crescent shaped assembly containing 26 hIAPP molecules and a smaller circular one containing 10 hIAPP had formed: at greater peptide concentration the overall size of the aggregates is larger.

Repeated simulations showed that hIAPP aggregates consisting of less than ~ 10 peptides preferred circular shapes and larger aggregates grew linearly to form crescent-like aggregates. We determined the basic stable structural unit to be a pentameric aggregate. Aggregate growth occurred through the formation of edge-fused pentameric clusters. This finding is in agreement with AFM experiments (both circular and pentameric aggregates have been observed) that have also indicated the possibility of a similar growth mechanism^{28,45}. Growth of hIAPP and rIAPP aggregates is shown in Fig. 2. We will discuss the physical mechanism determining the stability and shape of hIAPP aggregates later on.

Next, we compared the behavior of rIAPP (used here as a negative control) with hIAPP. As figure 1 show, hIAPP forms large aggregates (edge-fused pentameric assemblies). For rIAPP, the aggregate size appears to be limited and the preferred shape is more circular. Another important qualitative difference between hIAPP and rIAPP is that hIAPP peptides (monomers and assemblies) always

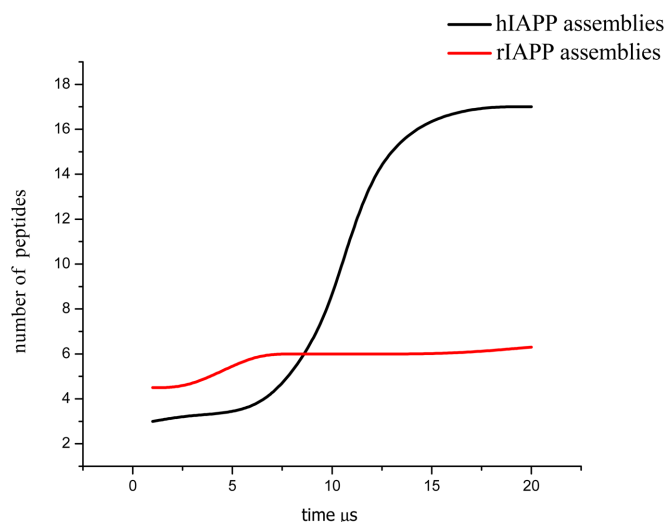


Figure 2 | hIAPP aggregation gives rise to larger peptide assemblies than rIAPP within a μ s timescale. Peptide aggregation in a POPC membrane as a function of time for 36 molecules of rIAPP and hIAPP in 20 μ s CG simulations.

stayed within the membrane, but rIAPP peptides moved out of the bilayer and emerged onto its surface. Upon moving toward the surface, the rIAPP peptides helped form membrane defects that allowed water to permeate into the bilayer. This behavior was always observed in repeated simulations.

The CG approach provides information about peptide and membrane dynamics, but not about the secondary structure of membrane-embedded hIAPP peptides. To study that, we performed extensive atomistic MD simulations of pentameric assemblies. First, a comparison of the hIAPP secondary structures at the beginning and at the end of the simulations showed that only residues 14 to 27 (sequence NFLVHSSNNFGAIL) remained α -helical. The rest partially unfolded to random coils. The secondary structure of the remaining residues in the assembly did not change during 0.3 μ s of atomistic MD simulations. This confirms the stability of hIAPP pentamers: No dissociation of pentamers or even an indication of any of the hIAPP peptides moving out of the membrane was seen in repeated simulations. The helical wheel representation of hIAPP in a pentameric assembly (Fig. 3) provides a qualitative explanation of their stability: Hydrophobic residues become oriented toward the surrounding lipids.

MD simulations of the pentameric assembly at 300 K did not reveal any tendency for the peptide to adopt β -sheet structures. These are traditionally considered the precursors of amyloid formation in solution, but not necessarily of oligomers interacting with membranes^{37,46,47}. To assess if the transition from α -helical to β -sheet structures is hindered by energy barriers, we carried out an additional 80 ns MD simulation at 400 K. Only a 1.8% increase in β -sheet content was observed.

Figure 4 illustrates an ion-channel like water permeable pore formed by five hIAPP peptides (in red). The pore allowed for water molecules to diffuse across the bilayer. Of the total 12 water molecules inside the hIAPP aggregate, four persisted inside for the entire 0.3 μ s. In the case of rIAPP (right panel), of the total 24, just one remained inside (hydrogen-bonded to the residues with a longer persistence). The main difference is the water molecules' distribution inside the pore: Water molecules inside the hIAPP pore appear to be confined in a restricted region because of the tight connections between peptides. For rIAPP, they are distributed randomly to fill the empty space generated by structural rearrangements of the replicas. We also performed 0.3 μ s full atomistic MD simulation of rIAPP

assemblies at 300 K. The lack of secondary structure stability is clearly evident, and α -helix/random coil/ β -turn conformational transitions occur at a higher rate as compared to hIAPP. Snapshots are shown in Figs. 4 and 5. The structural changes and motions of rIAPP peptides occurred through movement of the N-terminus (residues 1–15) across lipid-water interface. The observed differences between hIAPP and rIAPP are in agreement with NMR studies that show that hIAPP and rIAPP have very different orientations in a membrane⁴⁸.

The stability of the 10- and 26-meric hIAPP assemblies at the end of the CG simulation was addressed by setting up a 40 ns of all atom MD simulation at 300 K, using the configuration from the last frame of the 26 μ s CG simulation as the starting point. We performed an additional 20 ns all atom MD simulation at 400 K to help the system to overcome energy barriers hindering further association-dissociation events. For the first 40 ns, the α -helix content remained unchanged at about 11%. Water molecules were able to permeate through the 26-meric aggregate, but with a distinctly higher efficiency in comparison with the pentameric aggregate. We infer this to be due to the larger size and mobility of hIAPP aggregates. We then increased the temperature to 400 K for additional 20 ns and observed an increase in the β -sheet content from 3% to 9%.

Thermodynamic model for hIAPP self-assembly within lipid bilayer.

We developed a simple thermodynamic model to study the stability and morphological changes of hIAPP aggregates. The basic assumptions: 1) Aggregates may consist of i) isolated monomers, ii) pentagonal aggregates and iii) aggregates of edge-fused pentagons. Since fused pentagons can be formed by adding (one-by-one) three peptides to a pentagonal assembly, aggregates contain 5, 8, ... $3n + 2$, ... monomers. Smaller aggregates ($n < 5$) exist in dilute systems and are of not of interest here. 2) Two regular pentagons sharing a common edge are rotated by $\pi/5$ with respect to each other. Although regular pentagonal tiling is not space filling in two dimensions, to keep the model simple we did not take into account the factors arising from incomplete packing. 3) Equilibrium requires the chemical potential of peptides in different aggregates to be the same, $\mu_1 = \mu_5 = \mu_8 = \dots = \mu_{3n+2}$ and $\mu_1 = \mu_{3n+2}$ where μ_{3n+2} and μ_{3n+2} are the chemical potentials of linear and cyclic assemblies containing n and n^* fused pentagons, respectively. The general form of μ_{3n+2} is

$$\mu_{3n+2} = \mu_{3n+2}^0 + \frac{kT}{3n+2} \log \frac{X_{3n+2}}{3n+2}, \quad (1)$$

where X_j is the fraction of structures with aggregation number j , and μ_j^0 is the corresponding free energy per molecule. An analogous expression holds for μ_{3n^*+2} .

Each trimer forms 2 internal bonds with its own peptides and 4 bonds with the neighbouring trimers. The associated mean energy is $-6n\alpha$, where $-\alpha$ is the strength of each intermolecular bond. Due to the two free ends in a linear aggregate, and since there are 4 missing bonds at the ends, we have $U_{\text{BONDS}} = -(6n - 4)\alpha$.

The above is strictly local. To include non-local forces, we introduce electrostatics. Our MD simulations showed that the dipole moment of the hIAPP peptides is perpendicular to the membrane surface and in the range 300–500 D. This makes dipolar effects the most important interactions. Two identical parallel dipoles inserted into a lipid bilayer interact repulsively: $U_{\text{DIPOLE}}(|\mathbf{r} - \mathbf{r}'|) = + \frac{m_{\text{eff}}^2}{\epsilon a^3 (\mathbf{r} - \mathbf{r}')^3}$, where m_{eff} is the effective dipole moment of the protein repeat unit, ϵ is the bilayer dielectric permittivity and a is the mean distance between two nearby repeat units along the peptide. Summing over a line of n identical dipoles gives the dipolar energy (see Supplementary Material)

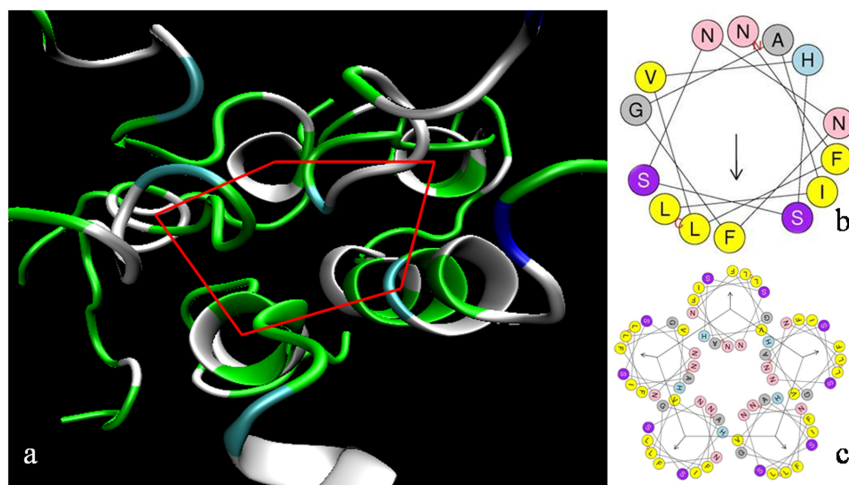


Figure 3 | Membrane-embedded hIAPP peptides associate into α -helical pentamers. (A) Pentameric assembly of membrane-bound hIAPP peptides obtained at the end of a 0.3 μ s MD simulation at 300 K. Green: polar, white: non-polar, cyan: polar ionizable. (B) Helical wheel representation of hIAPP side chains 14–27. (C) Pentameric aggregate. The vector in the xy -plane represents the hydrophobic moment⁸⁹. The helix dipole moment (not shown) is along the z -axis. Color code (b and c): yellow: hydrophobic (large), light blue: polar ionizable, magenta: polar; gray: hydrophobic (small); pink: polar.

$$\frac{1}{2} \int_S \int_{S'} \rho(\mathbf{r}) \rho(\mathbf{r}') U_{INTER}(|\mathbf{r} - \mathbf{r}'|) d\mathbf{r} d\mathbf{r}' \approx + n \frac{m_{eff}^2}{2\epsilon a^3} \left(1 - \frac{2}{n} + O(n^{-2}) \right). \quad (2)$$

where ρ the density per unit length. Adding $U_{BONDS} = -(6n - 4)\alpha$ and Equation (2), and dividing by the number of peptides in a generic aggregate $(3n + 2)$, we find an expression for the chemical potential:

$$\mu_{3n+2}^o \approx \frac{1}{3n+2} (-A + Bn) \quad \text{where} \quad (3a)$$

$$A \equiv 4\alpha - \frac{m_{eff}^2}{\epsilon a^3} \quad \text{and} \quad B \equiv 6\alpha - \frac{m_{eff}^2}{2\epsilon a^3}.$$

When the dipole is perpendicular to the membrane plane, self-assembly is hindered by competition with short-range adhesion forces. To trigger aggregation, we must have $4\alpha > \frac{m_{eff}^2}{\epsilon a^3}$. An analogous calculation for a cyclic aggregate made of n^* repeat units gives (see Supplementary Material)

$$\mu_{3n^*+2}^o \approx \frac{B^* n^*}{3n^*+2} \quad \text{with} \quad B^* \equiv 6\alpha - \frac{m_{eff}^2}{2\epsilon a^3} \left(1 + \left(\frac{\pi}{n^*} \right)^2 \log \left(\frac{2n^*}{\pi} \right) \right) \quad (3b)$$

The numerical values of A , B and B^* (in Equations. 3a and 3b) obey $A < B^* < B$.

Figure 6 shows that the chemical potential of the circular aggregate is almost independent of the aggregation number n , while that of an open aggregate decreases monotonously. At small n , circular aggregates are more stable than linear ones, but beyond a critical value the situation is reversed. This is a consequence of the non-local electrostatic interactions and it provides mechanism to relieve the electrostatic stress.

Combining the entropic and enthalpic contributions to the chemical potential (Equations 3a,b and 1) and equating the chemical potentials of the aggregate and free monomers, we calculate the concentrations of linear and cyclic aggregates $X_{3n+2} = (3n+2)X_1^2 (X_1^3 e^{B/kT})^n e^{-A/kT}$ and $X_{3n^*+2} = (3n^*+2)X_1^2 (X_1^3 e^{B^*/kT})^{n^*}$,

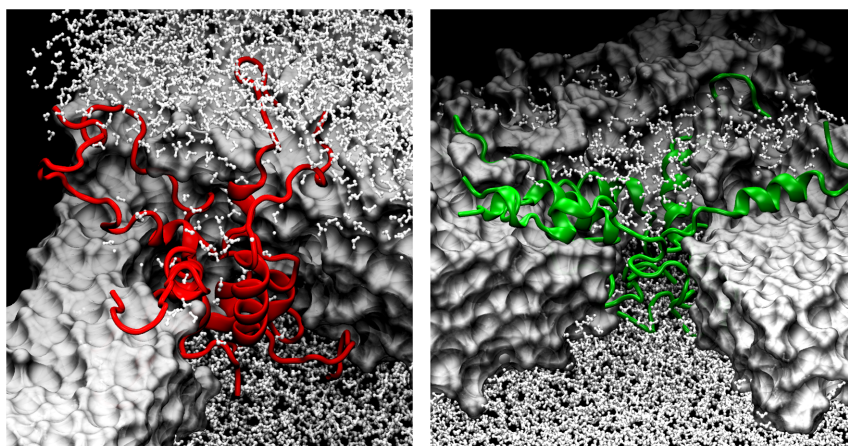


Figure 4 | hIAPP pentamers resemble barrel-shaped channels whereas the corresponding rIAPP assemblies look like loose funnels. Snapshots from AA-MD simulations of hIAPP (red) and rIAPP (green) pentamers after 300 ns. Color code: white-surf-lipids, white-CPK-water.

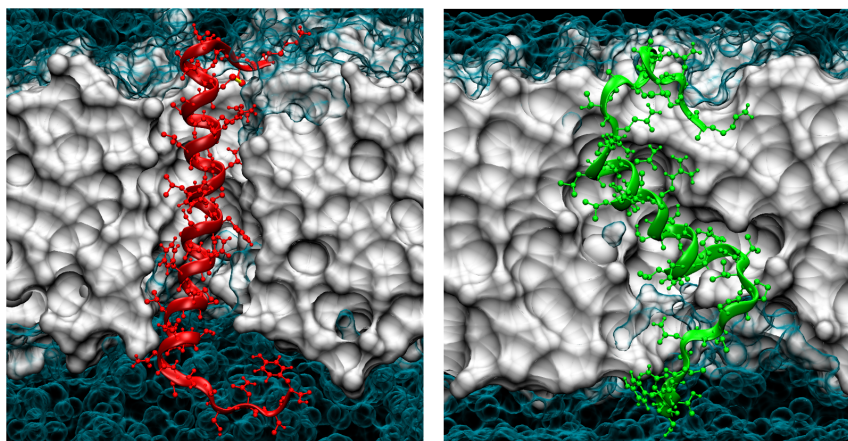


Figure 5 | Conformational preferences of monomeric hIAPP/rIAPP dictate the structural features of the pentameric assemblies. Snapshots of hIAPP (red) and rIAPP (green) at monomeric state after 40 ns of MD simulation. POPC lipids are shown in white and water molecules in cyan.

respectively. A , B and B^* are defined by Equations. (3a,b). Eliminating the still unknown monomer concentration X_1 by using mass conservation for peptides, we numerically calculated the fraction of linear and cyclic aggregates as a function of the total peptide concentration C . The plot of X_{CYCLIC}/X_{TOTAL} vs C is shown in the inset of Figure 6. At low concentrations, the fraction of cyclic aggregates is zero. At the critical protein concentration, C_{CYCLIC}^* , cyclic structures begin to form. Their concentration grows rapidly reaching a maximum at C_{CYCLIC}^{MAX} . The concentration of circular aggregates decreases slowly with protein concentration, long fibers being more favoured. The maximum becomes less pronounced and shifts toward higher concentrations upon increasing dipole moment.

The existence of an optimum size for cyclic structures is further reinforced if we use the notion of spontaneous curvature. As discussed at the beginning of this section, the repeat units of hIAPP aggregates are fused pentamers. Each unit introduces a spontaneous

bending of $\pi/5$. In order to form a closed circle, one must accommodate 10 fused pentamers (or 32 peptides). Such a structure has a zero internal strain, while larger or smaller cycles are less stable.

Kinetic control of the growing aggregate morphology. The simple model developed in the previous section relies on the assumption of a linear growth of the aggregate through continuous insertion of monomers at the growing free ends. MD simulations show a more complex mechanism involving a branching mechanism often observed in worm-like micellar systems⁴⁹. Branching strongly increases with local supersaturation, as also modelled in a recent paper⁵⁰. This parasitic process competes in a concentration-dependent way with the formation of closed regular toroids as discussed in the previous section. The formation of branched assemblies explains the slow and erratic kinetics of toroids birth and death in MD simulations we describe below.

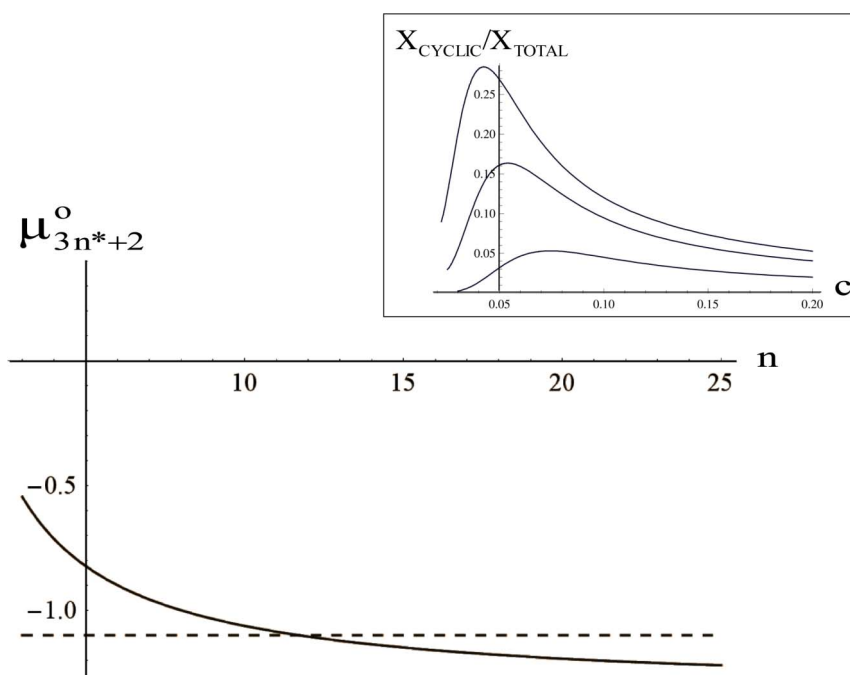


Figure 6 | Kinetics obtained from the thermodynamic model shows the transient nature of aggregates. Variation of the chemical potentials of linear (full line) and cyclic (dashed line) vs the aggregation number n . At the intersection, linear and cyclic aggregate have the same energy. *Inset:* Relative concentration of cyclic aggregates vs. the total protein concentration C . Curves have been calculated for different values of the temperature scaled dipolar energy $m_{eff}^2/\epsilon a^3 kT$. From the top to the bottom: $m_{eff}^2/\epsilon a^3 kT = 1, 2, 3$.



In order to verify if the distribution of the different aggregates is consistent with the prediction of our thermodynamic model, we performed a series of CG simulations at 300 K in the microsecond time range. Calculations were performed at different lipid/protein ratios (from 1/13 to 1/44). The most interesting outcomes were:

- The shape of the hIAPP aggregates is not linear. This feature is consistent with the notion of spontaneous curvature stemming from the pentameric geometry of the repeat units. Moreover, the growth of the aggregates exhibits frequent branching points, a clear indication of comparable lipid-peptide and peptide-peptide interactions (Fig. 7 b, c).
- Formation of closed toroids is a rare event. This observation is consistent with the large activation energy required to bend an aggregate made of self-repelling dipoles into a circle. High peptide concentrations favor closure (Fig. 7).
- Once the toroid has been closed, it is thermodynamically stable because the energy gain associated to the sealing of the two free ends. This process was investigated by leaving a closed toroid in contact with a dispersion of monomers (protein/lipid ratio 1/13) for 2 μ s at 300 K (Fig. 7d).

Membrane curvature generated by hIAPP assemblies. Insertion of a protein into a membrane perturbs lipid packing and results in local bending deformations. To minimize energetically unfavorable deformations, proteins tend to cluster⁵¹. These elastic forces have to be added to other contributions such as hydrophobicity and electrostatics to understand the origin of protein aggregation in membranes. The intricate coupling between shape and aggregation has been studied both analytically⁵² and computationally⁵³. When the bilayer-spanning impurity is anisotropic (e.g. wedge shaped), geometric anisotropy induces anisotropic interactions among the impurities resulting in linear rather than globular aggregates^{54,55}.

Curvature stress has been suggested to account for the early stages of hIAPP-mediated membrane damage^{56–58}.

hIAPP aggregates have a semi-toroid structure with cone-shaped cross-section (top side depth of about 43 Å and down side depth of about 22 Å), mainly due to the electrostatic repulsions between charges localized in the water-exposed region of the outer monolayer. Cone shapes have also been indicated in aggregates of amyloid β ⁵¹. This geometry suggests a considerable aggregate-membrane bending coupling. The MD simulation of the 26-meric hIAPP assembly performed at 400 K showed significant curvature stress induced by the aggregate as shown in Fig. 8. This geometry can be explained by considering the electrostatic repulsions of the positively charged residues in the same side of the bilayer. We observed an increase in membrane fluctuations along the z -axis in the MD simulations of 26 hIAPP molecules.

Although the experimental data reported in Fig. 9 involve larger time and space scales than those investigated by our MD simulations, results are fully consistent. Well-founded analytical theories for the shape of multi-component vesicles predict a sphere to ellipsoid transition due to the segregation of the component with the greatest intrinsic curvature in the more curved regions of the vesicle⁵⁹. The effect is enhanced in the case of strong incompatibility among the two vesicles components (segregation). Both incompatibility and spontaneous bilayer curvature were observed in all atoms simulations in the case of hIAPP but not with rIAPP.

Discussion

Previous theoretical considerations of oligomer and fibril growth in aqueous solutions have revealed some of the general principles governing the transition from monomeric proteins to ordered fibrillar aggregates^{60–62}. However, increasing evidence supports the hypothesis that hIAPP permeabilizes membranes either through the formation of pores or through detergent-like damage of the bilayer.

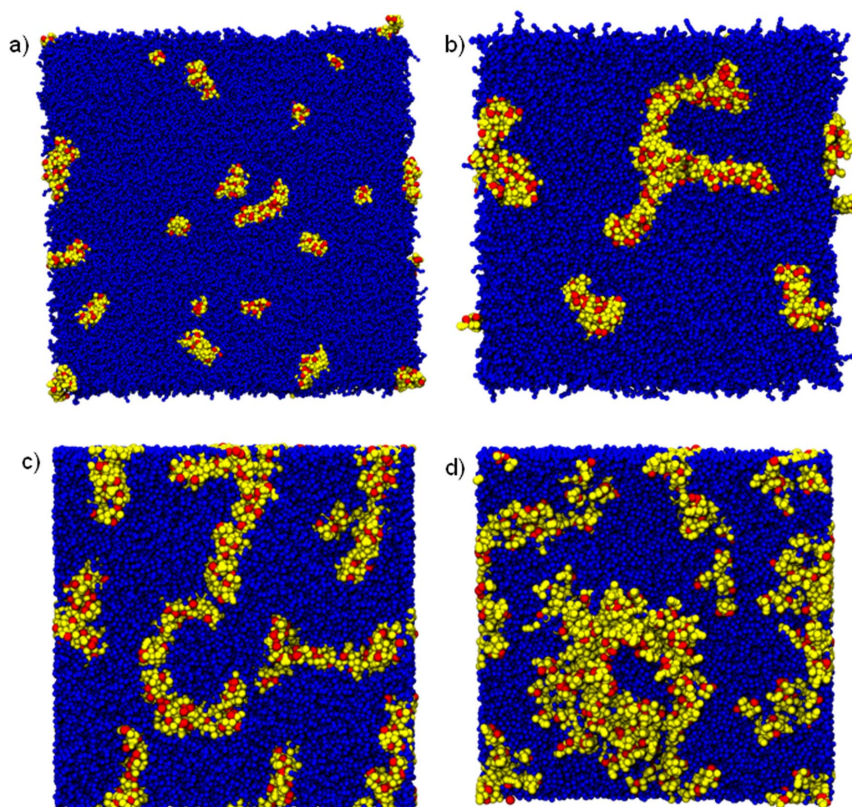


Figure 7 | (a) snapshot at 10 μ s (protein/lipid ratio 1/44); (b) snapshot at 8 μ s (protein/lipid ratio 1/19); (c) snapshot at 6 μ s (protein/lipid ratio 1/24); (d) snapshot taken after 1 μ s from the toroid formation (protein/lipid ratio 1/13).

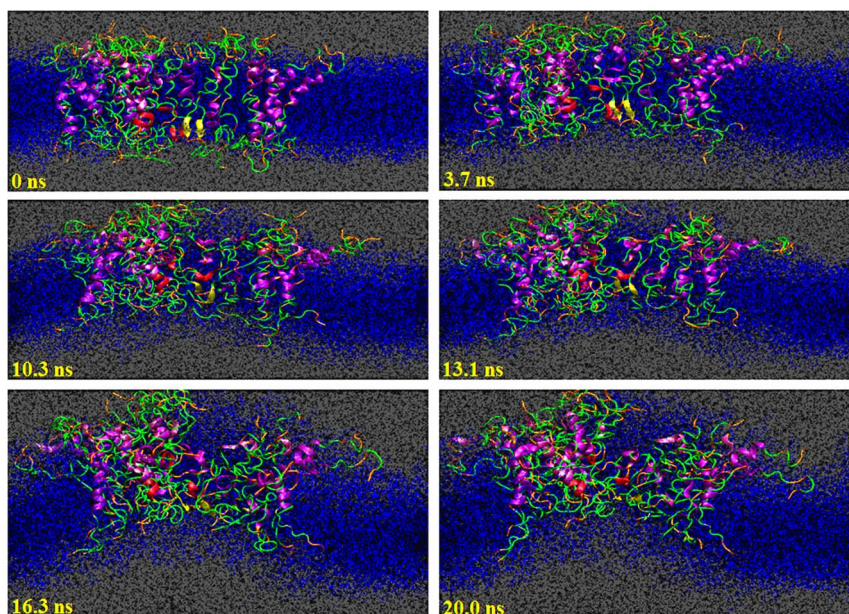


Figure 8 | Annular cone-shaped hIAPP assemblies cause membrane curvature. Snapshots (cross-section) from the MD simulation of 26 hIAPP molecules in POPC bilayer at 400 K.

These mechanisms are not mutually exclusive. A recent report suggested a leakage mechanism wherein a porous protein aggregate is formed by stochastic nucleation of hIAPP molecules⁶³. Such states have been referred to as less structurally defined chaotic pores^{64,65}, a view reconcilable with the nonspecific nature of channel-like aggregates.

Our atomistic simulations performed at the critical intermediate steps along the CG simulation allowed: i) the capture of the structural details about the relevant intermediate peptide assemblies, and ii) construction of a thermodynamic model to study the importance of dipole interactions in determining size and morphology of the aggregates. CG simulations provided a mechanistic description of the interactions of transmembrane α -helices with lipid bilayers⁶⁶ as well as evidence that a water-permeable pentameric assembly of hIAPP α -helices is a critical intermediate towards reconciliation with the predictions of the proposed thermodynamic model. The number of helices constituting the pore as well as its effective diameter predicted from our simulations are in agreement with previous experimental studies^{28,38}. The multiscale approach allowed us to study the detailed

mechanisms and to develop a minimal thermodynamic model for analysing the transient nature of toroidal aggregates and aggregate shapes. The balance among concentration-related entropy, unfavorable edge effects of a self-assembled small aggregates and repulsive dipolar interactions among the dipoles make the circular aggregates a metastable state that can be observed only in a narrow window of protein/lipid ratios. At lower concentrations smaller oligomers (from monomers to pentamers) prevail, while at higher values fibrils dominate over the toroidal aggregates.

The predictions of the model when compared with CG simulations by increasing hIAPP concentration above the threshold protein concentration showed that hIAPP pentamers spontaneously evolve into a large cyclic assembly.

Importantly, this structure is able to render the membrane water-permeable and, concomitantly, to induce significant curvature into the membrane. It is tempting to speculate that this assembly may involve more than one peptide-based mechanisms for membrane-damage, but a conclusive demonstration would require a separate study. Parallel simulations performed on the non-toxic,

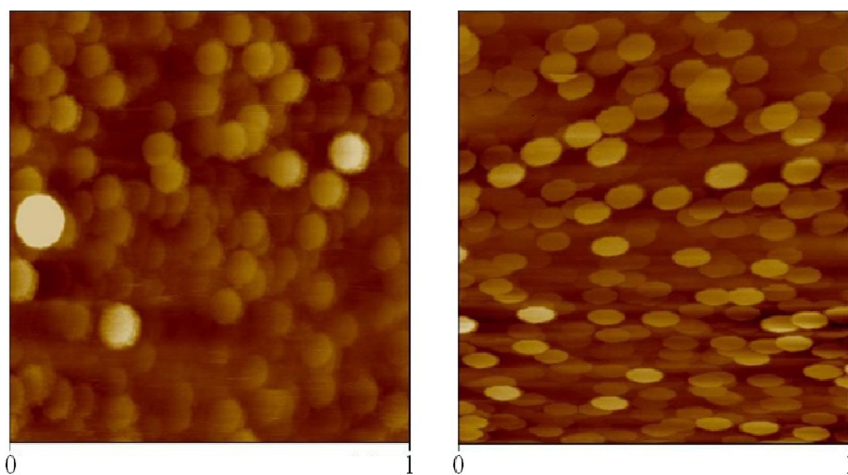


Figure 9 | AFM in liquid of 1 μm^2 containing POPC/POPS (95/5 molar ratio) LUVs. Left panel: imagine of vesicles in PBS buffer. Right panel: imagine of vesicles after incubation with hIAPP 5 μM . rIAPP did not show induce any changes in the vesicles shape (not shown).



non-amyloidogenic rat derivative rIAPP were significantly different from hIAPP: No compact ordered large aggregates were observed (Fig. 1).

There are also some important differences between our CG simulations and experimental observations previously reported. First, the time scale of the events: Experimental measurements require an initial diffusion to the membrane surface, and could be rate-determining (peptides are inserted into the membrane). The second difference is that the relatively small size of our system precludes the observation of large long-lived pores or other breakage mechanisms in the membrane. Thus, the increase in permeability of water and ions observed in our simulations may be a prelude to a multifaceted disruption of the membrane.

Most of the studies thus far have focussed on dimer formation, typically by investigating IAPPs in solutions^{31–33}. Two recent computational studies using very different methods have, however, suggested the importance of trimers^{67,68}. Our analytical model shows how trimers are *the most important building blocks* in the formation of the stable fused pentameric superstructures. Our CG simulations confirm this mechanism.

Finally, using the structural differences between hIAPP and rIAPP observed in MD simulations, we speculate that α -helices may be the dominant structure under certain conditions. Using a simple model, Dias et al.⁶⁹ have shown that β -sheets, since they have the ability to lower hydrophobic energy, tend to be the favored ones in solution – this has also been seen in many simulations^{31–35}. In a membrane environment, however, the free energy difference between α -helices and β -sheet may become much smaller, although the conformations are separated by free energy barrier that can be large; here, we saw only a small increase in β -sheet formation even at an elevated temperature. This is in excellent agreement with the fluorescence correlation spectroscopy experiments of Magzoub and Miranker⁷⁰ who found that in membranes, IAPPs prefer α -helices over β -sheet, and that toxicity is related to the α -helical conformations. hIAPP is able to form aggregates that minimize the hydrophobic mismatch with the bilayer and peptide-peptide H-bonds that stabilize the pore and allow for a small number of waters to penetrate. Such stabilization mechanism does not exist for rIAPP and hence the peptides escape to the membrane surface. The stability of hIAPP assemblies also allows for diffusion of ions through the channel that may disrupt ion homeostasis and contribute to neuronal death as has been suggested in the case of amyloid- β ⁷¹. Whether or not the hIAPP channel is selective remains a topic for future studies.

Methods

We performed a combination of coarse grained (CG) and atomistic molecular dynamics (MD) simulations at 300, 350 and 400 K. Reverse mapping⁷² was used to connect the different length scales. This protocol allowed for longer simulation times and detailed studies of the different intermediate states. The NMR structures of hIAPP bound to sodium dodecylsulfate (SDS) micelles (pdb ID: 2KB8)⁷³ and rIAPP in dodecylphosphocholine (DPC) micelles (pdb ID: 2KJ7)⁷⁴ were first energy minimized using the method of steepest descents (the first structures in the PDB files were used). Pre-equilibration was done using atomistic MD in the NVT ensemble. This was followed by an equilibration simulation run of 40 ns. All simulations, CG and MD, were carried out using Gromacs 4⁷⁵ software and methodological issues⁷⁶ related to neighborlist updates and charge groups were taken into account. GROMOS 53A6⁷⁷ force field was used in all atomistic MD. This force-field has been shown to perform well in simulations of membrane-protein systems^{78,79}. Coarse-grained models based on the MARTINI^{80–82} force field were constructed based on the final conformations.

For the lipid bilayer, a pre-equilibrated (100 ns) 128 lipid POPC membrane⁸³ hydrated by 1500 water molecules was used as a starting point. This bilayer was replicated to obtain a membrane with 1596 lipids, energy minimized by the steepest descent algorithm (1000 steps), and equilibrated in the NpT ensemble for 100 ns. Finally, systems consisting of rIAPP or hIAPP and a bilayer were constructed. Peptides were inserted inside the membrane perpendicularly to the membrane surface using Gromacs tool `gmx insert_molecules`. The box containing a single protein was then replicated and the lateral size adjusted to achieve the desired concentration. The CG systems were hydrated by ~23,000 water molecules in the presence of 0.1 M NaCl. Cl⁻ counterions were added to preserve charge neutrality. This system was again energy minimized by the steepest descent algorithm and equilibrated in the NpT ensemble for 100 ns. The starting configurations were obtained by extracting a portion of the

bilayer containing the corresponding structure, maintaining the same protein/lipid ratio, from the CG simulation; a section of the bilayer within a specified radius from the center of mass of a chosen aggregate was cut and reverted to an atomistic representation. As for pentamers, we selected and reverted three different aggregates to test the reproducibility of the structural properties investigated. Peptide chains had same orientations (in agreement with NMR experiments showing the tendency of the single peptide to penetrate in membrane through the N-terminal).

In atomistic MD, the SPC (simple point charge) water model⁸⁴ was used. The time step was set to 1 fs and the temperature was kept constant using the Nose-Hoover algorithm^{85,86} with a time constant of 0.1 ps. Periodic boundary conditions were applied. The Parrinello-Rahman algorithm⁸⁷ was applied for semi-isotropic pressure coupling (1 bar). The particle-mesh Ewald (PME) algorithm⁸⁸ was used for electrostatics. In the CG simulations, we used the Berendsen weak coupling thermostat and barostat algorithms⁸⁹ with coupling constants of 0.3 ps and 3.0 ps, respectively. The following CG-systems were used in production runs: 36 hIAPP/rIAPP peptides for 26 μ s at 300 K. A 13 μ s simulation at 300 K with 104 peptides. Several concentration ratios protein/lipids have been also tested (1 : 13, 1 : 19, 1 : 24, 1 : 44).

MD production runs were as follows: Monomeric hIAPP or rIAPP embedded in a POPC membrane was simulated for 40 ns. Pentameric hIAPP/rIAPP assemblies obtained at the end of 6 μ s CG simulation were simulated at 300 K for 0.3 μ s. The temperature was increased to 400 K for 80 ns. hIAPP semi-toroidal 10-meric and the hIAPP semi-toroidal 26-meric aggregates were simulated for 40 ns at 300 K. The structure at the end of 26 μ s CG simulation was simulated. The temperature was increased to 400 K for 20 ns (after 40 ns at 300 K).

Atomic Force Microscopy (AFM) measurements were performed in liquid at room temperature using a Digital Instruments nanoscope, model IIIa. Images were acquired in tapping mode with a fluid cell filled with phosphate buffer solution (pH 7.4, 100 mM NaCl). Where present, hIAPP or rIAPP concentration was 5 μ M. Model membranes, containing a mixture of 1,2-palmitoil-oleil-sn-glycero-3-phosphocholine (POPC) and 1,2-palmitoil-oleil-sn-glycero-3-phospho-L-serine (POPS) (molar ratio 95/5) were prepared as described elsewhere⁵⁷. The choice of this lipid composition is critical to prevent the formation of a Supported Lipid bilayer (planar bilayer) and to keep the LUVs intact although they are bound to the silica surface.

- Merlini, G. & Bellotti, V. Molecular mechanisms of amyloidosis. *N. Engl. J. Med.* **349**, 583–596 (2003).
- Hardy, J. & Selkoe, D. J. The amyloid hypothesis of Alzheimer's disease: progress and problems on the road to therapeutics. *Science* **297**, 353–356 (2002).
- Dickson, D. W. The pathogenesis of senile plaques. *J. Neuropathol. Exp. Neurol.* **56**, 321–339 (1997).
- Abedini, A. & Raleigh, D. P. A role for helical intermediates in amyloid formation by natively unfolded polypeptides? *Phys. Biol.* **6**, 015005 (2009).
- Miller, Y., Ma, B. & Nussinov, R. Polymorphism in Alzheimer Abeta amyloid organization reflects conformational selection in a rugged energy landscape. *Chem. Rev.* **110**, 4820–4838 (2010).
- Dupuis, N. F., Wu, C., Shea, J. & Bowers, M. T. Human islet amyloid polypeptide monomers form ordered beta-hairpins: a possible direct amyloidogenic precursor. *J. Am. Chem. Soc.* **131**, 18283–18292 (2009).
- Bernstein, S. L. et al. Amyloid- β protein oligomerization and the importance of tetramers and dodecamers in the aetiology of Alzheimer's disease. *Nature Chem.* **1**, 326–331 (2009).
- Hoppener, J. W., Ahren, B. & Lips, C. J. Islet amyloid and type 2 diabetes mellitus. *N. Engl. J. Med.* **343**, 411–19 (2000).
- Kahn, S. E., Andrikopoulos, S. & Verchere, C. B. Islet amyloid: a long-recognized but underappreciated pathological feature of type 2 diabetes. *Diabetes* **48**, 241–253 (1999).
- Haataja, L., Gurlo, T., Huang, C. J. & Butler, P. C. Islet amyloid in type 2 diabetes, and the toxic oligomer hypothesis. *Endocr. Rev.* **29**, 303–316 (2008).
- Ramamoorthy, A. & Lim, M. H. Structural Characterization and Inhibition of Toxic Amyloid- β Oligomeric Intermediates. *Biophys. J.* **105**, 287–288 (2013).
- Milojevic, V. & Melacini, V. Stoichiometry and Affinity of the Human Serum Albumin-Alzheimer's A β Peptide Interactions. *Biophys. J.* **100**, 183–192 (2011).
- Raditsis, V., Milojevic, V. & Melacini, V. A β Association Inhibition by Transferrin. *Biophys. J.* **105**, 473–480 (2013).
- Glabe, C. G. Common mechanisms of amyloid oligomer pathogenesis in degenerative disease. *Neurobiol. of aging*. **4**, 570–575 (2006).
- Kayed, R. et al. Common structure of soluble amyloid oligomers implies common mechanism of pathogenesis. *Science* **300**, 486–489 (2003).
- Demmester, N. et al. Apoptosis induced in neuronal cells by C-terminal amyloid fragments is correlated with their aggregation properties in phospholipid membranes. *Mol. Membr. Biol.* **17**, 219–228 (2000).
- Kawahara, M., Kuroda, Y., Arispe, N. & Rojas, E. Alzheimer's amyloid, human islet amylin, and prion peptide fragment evoke intracellular free calcium elevations by a common mechanism in a hypothalamic GnRH neuronal cell line. *J. Biol. Chem.* **275**, 14077–14083 (2000).
- Lin, H., Bhatia, R. & Lal, R. Amyloid protein forms ion channels: implications for Alzheimer's disease pathology. *FASEB J.* **15**, 2433–2444 (2001).
- Hebda, J. A. & Miranker, A. D. The interplay of Catalysis and Toxicity by Amyloid intermediates on Lipid Bilayers: Insights from Type II Diabetes. *Ann. Rev. Biophys.* **38**, 125–152 (2009).



20. Sciacca, M. F. *et al.* Two-Step Mechanism of Membrane Disruption by Ab through Membrane Fragmentation and Pore formation. *Biophys. J.* **103**, 702–710 (2012).
21. Butterfield, S. M. & Lashuel, H. Amyloidogenic protein-membrane interactions: mechanistic insight from model systems. *Angew. Chem.* **49**, 5628–5654 (2010).
22. Brender, J. R. *et al.* Amyloid Fiber Formation and Membrane Disruption are Separate Processes Localized in Two Distinct Regions of IAPP, the Type-2-Diabetes-Related Peptide. *J. Am. Chem. Soc.* **130**, 6424–6429 (2008).
23. Sciacca, M. F. M. *et al.* Cations as Switches of Amyloid-Mediated Membrane Disruption Mechanisms: Calcium and IAPP. *Biophys. J.* **104**, 172–184 (2013).
24. Brender, J. R., Salamekh, S. & Ramamoorthy, A. Membrane Disruption and Early Events in the Aggregation of the Diabetes Related Peptide IAPP from a Molecular Perspective. *Acc. Chem. Res.* **45**, 454–462 (2012).
25. Cooper, G. J. *et al.* Purification and characterization of a peptide from amyloid-rich pancreases of type 2 diabetic patients. *Proc. Natl. Acad. Sci. USA* **84**, 8628–8632 (1987).
26. Westermark, P., Andersson, A. & Westermark, G. T. Islet amyloid polypeptide, islet amyloid, and diabetes mellitus. *Physiol. Rev.* **91**, 795–826 (2011).
27. Harroun, T. A., Bradshaw, J. P. & Ashley, R. H. Inhibitors can arrest the membrane activity of human islet amyloid polypeptide independently of amyloid formation. *FEBS. Lett.* **507**, 200–204 (2001).
28. Hirakura, Y., Yiu, W. W., Yamamoto, A. & Kagan, B. L. Amyloid peptide channels: blockade by zinc and inhibition by Congo red (amyloid channel block). *Amyloid* **7**, 194–199 (2000).
29. Mirzabekov, T. A., Lin, M. C. & Kagan, B. L. Pore formation by the cytotoxic islet amyloid peptide amylin. *J. Biol. Chem.* **271**, 1988–1992 (1996).
30. Anguiano, M., Nowak, R. J. & Lansbury, P. T. Protofibrillar islet amyloid polypeptide permeabilizes synthetic vesicles by a pore-like mechanism that may be relevant to type II diabetes. *Biochemistry* **41**, 11338–11343 (2002).
31. Kawahara, M., Kuroda, Y., Arispe, N. & Rojas, E. Alzheimer's beta-amyloid, human islet amylin, and prion protein fragment evoke intracellular free calcium elevations by a common mechanism in a hypothalamic GnRH neuronal cell line. *J. Biol. Chem.* **275**, 14077–14083 (2000).
32. Weise, K., Radovan, D., Gohlke, A., Opitz, N. & Winter, R. Interaction of hIAPP with model raft membranes and pancreatic beta-cells: cytotoxicity of hIAPP oligomers. *ChemBioChem* **11**, 1280–1290 (2010).
33. Meier, J. J. *et al.* Inhibition of human IAPP fibril formation does not prevent beta-cell death: evidence for distinct actions of oligomers and fibrils of human IAPP. *Am. J. Physiol. Endocrinol. Metab.* **291**, E1317–24 (2006).
34. Nath, A., Miranker, A. D. & Rhoades, E. A membrane-bound antiparallel dimer of rat islet amyloid polypeptide. *Angew. Chem.* **50**, 10859–10862 (2011).
35. Quist, A. *et al.* Amyloids form membrane pores: a common structural link for protein-misfolding disease. *Proc. Natl. Acad. Sci. USA* **102**, 10427–10432 (2005).
36. Engel, M. F. M. *et al.* Islet amyloid polypeptide inserts into phospholipid monolayers as monomer. *J. Mol. Biol.* **356**, 783–789 (2006).
37. Prakash, R., Nanga, R. P. R., Brender, J. R., Vivekanandan, S. & Ramamoorthy, A. Structure and membrane orientation of IAPP in its natively amidated form at physiological pH in a membrane environment. *Biochim. Biophys. Acta* **1808**, 2337–2342 (2011).
38. Laghaei, R., Mousseau, N. & Wei, G. Effect of the disulfide bond on the monomeric structure of human amylin studied by combined Hamiltonian and temperature replica exchange molecular dynamics simulations. *J. Phys. Chem. B* **114**, 7071–7077 (2010).
39. Dupuis, N. F., Wu, C., Shea, J. E. & Bowers, M. T. The amyloid formation mechanism in human IAPP: dimers have β -strand monomer-monomer interfaces. *J. Am. Chem. Soc.* **133**, 7240–7243 (2011).
40. Reddy, A. S. *et al.* Stable and metastable states of human amylin in solution. *Biophys. J.* **99**, 2208–2216 (2010).
41. Andrews, M. N. & Winter, R. Comparing the structural properties of human and rat islet amyloid polypeptide by MD computer simulations. *Biophys. Chem.* **156**, 43–50 (2011).
42. Rivera, E., Straub, J. & Thirumalai, D. Sequence and crowding effects in the aggregation of a 10-residue fragment derived from islet amyloid polypeptide. *Biophys. J.* **96**, 4552–4560 (2009).
43. Xu, W., Wei, G., Su, H., Nordenskiöld, L. & Mu, Y. Effects of cholesterol on pore formation in lipid bilayers induced by human islet amyloid polypeptide fragments: A coarse-grained molecular dynamics study. *Phys. Rev. E* **84**, 1–8 (2011).
44. Lee, C., Sun, Y. & Huang, H. W. How Type II Diabetes-Related Islet Amyloid Polypeptide Damages Lipid Bilayers. *Biophys. J.* **102**, 1059–1068 (2012).
45. Scalisi, S. *et al.* Self-Assembling Pathway of HiApp Fibrils within Lipid Bilayers. *ChemBioChem* **11**, 1856–1859 (2010).
46. Sajith, A., Jayasinghe, S. A. & Langen, R. Membrane interaction of islet amyloid polypeptide. *Biochim. Biophys. Acta* **1768**, 2002–2009 (2007).
47. Soong, R., Brender, J. R., Macdonald, P. M. & Ramamoorthy, A. Association of Highly Compact Type II Diabetes Related Islet Amyloid Polypeptide Intermediate Species at Physiological Temperature Revealed by Diffusion NMR Spectroscopy. *J. Am. Chem. Soc.* **131**, 7079–7085 (2009).
48. Nanga, R. P. R., Brender, J. R., Xu, J., Veglia, G. & Ramamoorthy, A. Structures of Rat and Human Islet Amyloid Polypeptide IAPP1-19 in Micelles by NMR Spectroscopy. *Biochemistry* **47**, 12689–12697 (2008).
49. Oelschlaeger, C., Schopferer, M., Scheffold, F. & Willenbacher, N. Linear-to-Branched Micelles Transition: A Rheometry and Diffusing Wave Spectroscopy (DWS) Study. *Langmuir* **25**, 716–723 (2009).
50. Tang, M. & Carter, W. C. Branching Mechanisms in Surfactants Micellar Growth. *J. Phys. Chem. B* **117**, 2898–2905 (2013).
51. Pannuzzo, M., Milardi, D., Raudino, A., Karttunen, M. & La Rosa, C. Analytical model and multiscale simulations of A β peptide aggregation in lipid membranes: towards a unifying description of conformational transitions, oligomerization and membrane damage. *Phys. Chem. Chem. Phys.* **15**, 8940–8951 (2013).
52. Zimmerberg, J. & Kozlov, M. M. How proteins produce cellular membrane curvature. *Nature Rev. Mol. Cell. Biol.* **7**, 9–19 (2006).
53. Bahrami, A. H. & Jalali, M. A. Vesicle deformations by clusters of transmembrane proteins. *J. Chem. Phys.* **134**, 085106 (2011).
54. Dommersnes, P. G. & Fournier, J. B. N-body study of anisotropic membrane inclusions: Membrane mediated interactions and ordered aggregation. *Eur. Phys. J. B.* **12**, 9–12 (1999).
55. Igljic, A. *et al.* On the role of anisotropy of membrane constituents in formation of a membrane neck during budding of a multicomponent membrane. *J. Biomech.* **40**, 579–585 (2007).
56. Ramamoorthy, A., Thenarasu, S., Lee, D.-K., Tan, A. & Maloy, L. Solid-State NMR investigation of the membrane-disrupting mechanism of antimicrobial peptides MSI-78 and MSI-594 derived from magainin 2 and melittin. *Biophys. J.* **91**, 206–216 (2006).
57. Sciacca, M. F. M., Pappalardo, M., Milardi, D., Grasso, D. M. & La Rosa, C. Calcium-activated membrane interaction of the islet amyloid polypeptide: Implications in the pathogenesis of type II diabetes mellitus. *Arch. Biochem. Biophys.* **477**, 291–298 (2008).
58. Sciacca, M. F. M. *et al.* Are fibril growth and membrane damage linked processes? An experimental and computational study of IAPP(12–18) and IAPP(21–27) peptides. *New J. Chem.* **34**, 200–207 (2010).
59. Seifert, U. & Lipowsky, R. The morphology of vesicles. In Lipowsky, R. & Sackmann, E. editors "Structure and Dynamics of Membranes." p.403–463. Elsevier, Amsterdam (1995).
60. Straub, J. E. & Thirumalai, D. Toward a molecular theory of early and late events in monomer to amyloid fibril formation. *Ann. Rev. Phys. Chem.* **62**, 437–463 (2011).
61. Pappalardo, M. *et al.* A molecular dynamics study on the conformational stability of prp 180–193 helix ii prion fragment. *Chem. Phys. Lett.* **390**, 511–516 (2004).
62. Milardi, D., Pappalardo, M., Pannuzzo, M., La Rosa, C. & Grasso, D. M. The role of the Cys2-Cys7 disulfide bridge on the early steps of Islet Amyloid Polypeptide aggregation. *Chem. Phys. Lett.* **463**, 396–399 (2008).
63. Last, N. B., Rhoades, E. & Miranker, A. D. Islet amyloid polypeptide demonstrates a persistent capacity to disrupt membrane integrity. *Proc. Natl. Acad. Sci. USA* **108**, 9460–9465 (2011).
64. Gregory, S. M., Cavenaugh, A., Journigan, V., Pokorny, A. & Almeida, P. F. F. A quantitative model for the all-or-none permeabilization of phospholipid vesicles by the antimicrobial peptide cecropin A. *Biophys. J.* **94**, 1667–1680 (2008).
65. Axelsen, P. H. A chaotic pore model of polypeptide antibiotic action. *Biophys. J.* **94**, 1549–1550 (2008).
66. Bond, P. & Sansom, M. S. P. Insertion and assembly of membrane proteins via simulation. *J. Am. Chem. Soc.* **128**, 2697–2704 (2006).
67. Zhao, J., Yu, X., Liang, G. & Zheng, J. Heterogeneous triangular structures of human islet amyloid polypeptide (amylin) with internal hydrophobic cavity and external wrapping morphology reveal the polymorphic nature of amyloid fibrils. *Biomacromolecules* **12**, 1781–94 (2011).
68. Mo, Y., Lu, Y., Wei, G. & Derreumaux, P. Structural diversity of the soluble trimers of the human amylin(20–29) peptide revealed by molecular dynamics simulations. *J. Chem. Phys.* **130**, 125101 (2009).
69. Dias, C. L., Karttunen, M. & Chan, H. S. Hydrophobic interactions in the formation of secondary structures in small peptides. *Phys. Rev. E* **84**, 041931 (2011).
70. Magzoub, J. & Miranker, A. D. Concentration-dependent transitions govern the subcellular localization of islet amyloid polypeptide. *FASEB J.* **26**, 1228 (2012).
71. Yu, S. P., Farhangrazi, Z. S., Ying, H. S., Yeh, C.-H. & Choi, D. W. Enhancement of Outward Potassium Current May Participate in β -Amyloid Peptide-Induced Cortical Neuronal Death. *Neurobiol. Dis.* **5**, 81–88 (1998).
72. Rzepiela, *et al.* Reconstruction of atomistic details from coarse grained structures. *J. Comp. Chem.* **31**, 1333–1343 (2010).
73. Patil, S. M., Xu, S., Shefic, S. R. & Alexandrescu, A. T. Dynamic alpha-helix structure of micelle-bound human amylin. *J. Biol. Chem.* **284**, 11982–11991 (2009).
74. Nanga, R. P. R. *et al.* Three-dimensional structure and orientation of rat islet amyloid polypeptide protein in a membrane environment by solution NMR spectroscopy. *J. Am. Chem. Soc.* **131**, 8252–8261 (2009).
75. Hess, B., Kutzner, C., Van der Spoel, D. & Lindahl, E. GROMACS 4: Algorithms for Highly Efficient, Load-Balanced, and Scalable Molecular Simulation. *J. Chem. Theory. Comput.* **4**, 435–447 (2008).
76. Wong-ekkabut, J., Miettinen, M. S., Dias, C. & Karttunen, M. Static charges cannot drive a continuous flow of water molecules through a carbon nanotube. *Nature Nanotech.* **5**, 555–557 (2010).
77. Oostenbrink, C., Soares, T. A., van der Vegt, N. F. & van Gunsteren, W. F. Validation of the 53A6 GROMOS force field. *Biophys. J.* **34**, 273–284 (2005).



78. Wong-ekkabut, J. & Karttunen, M. Assessment of common simulation protocols for simulations of nanopores, membrane proteins & channels. *J. Chem. Theory Comput.* **8**, 2905–2911 (2012).
79. Cino, E. A., Choy, W.-Y. & Karttunen, M. Comparison of secondary structure formation using 10 different force fields in microsecond molecular dynamics simulations. *J. Chem. Theory Comput.* **8**, 2725–2740 (2012).
80. Monticelli, L. *et al.* The MARTINI coarse grained force field: extension to proteins. *J. Chem. Theory Comput.* **4**, 819–834 (2008).
81. Marrink, S. J., Risselada, H. J., Yefimov, S., Tieleman, D. P. & de Vries, A. H. The MARTINI forcefield: coarse grained model for biomolecular simulations. *J. Phys. Chem. B* **111**, 7812–7824 (2007).
82. Marrink, S. J., de Vries, A. H. & Mark, A. E. Coarse grained model for semi-quantitative lipid simulations. *J. Phys. Chem. B* **108**, 750–760 (2004).
83. de Jong, D. H., Singh, G., Bennett, W. F. D., Arnarez, C., Wassenaar, T. A., Schäfer, L. V., Periole, X., Tieleman, D. P. & Marrink, S. J. Improved parameters for the Martini coarse-grained protein force field. *J. Chem. Theory Comput.* **9**, 687–697 (2013). Parameters at <http://md.chem.rug.nl/cgmartini/index.php/force-field-parameters/lipids>.
84. Berendsen, H. J. C., Postma, J. P. M., van Gunsteren, W. F. & Hermans, J. *Interaction Models for Water in Relation to Protein Hydration*, in *Intermolecular Forces*, edited by Pullman, B. 331–342 D. Reidel Publishing Company, Dordrecht (1981).
85. Nosé, S. A. Unified formulation of the constant temperature molecular dynamics methods. *J. Chem. Phys.* **81**, 511 (1984).
86. Hoover, W. Canonical dynamics: Equilibrium phase-space distributions. *Phys. Rev. A* **31**, 1695–1697 (1985).
87. Parrinello, M. & Rahman, A. Polymorphic transitions in single crystals: A new molecular dynamics method. *J. Appl. Phys.* **52**, 7182–7190 (1981).
88. Darden, T., York, D. & Pedersen, L. Particle mesh Ewald: An Nlog(N) method for Ewald sums in large systems. *J. Chem. Phys.* **98**, 10089 (1993).
89. Berendsen, H. J. C., Postma, J. P. M., van Gunsteren, W. F., DiNola, A. & Haak, J. R. Molecular dynamics with coupling to an external bath. *J. Chem. Phys.* **81**, 3684–3690 (1984).

Acknowledgments

We thank NSERC of Canada (MK) and the Ontario Early Researcher Award Program (MK) for financial support. SharcNet [www.sharcnet.ca] and CINECA (Bologna, Italy) are acknowledged for computational resources. We thank Prof. Luisa D'Urso for AFM measurements.

Author contributions

M.K., C.L.R., A.R., D.M. and M.P. designed the experiments, performed the analysis and wrote the manuscript. M.P. performed the simulations.

Additional information

Supplementary information accompanies this paper at <http://www.nature.com/scientificreports>

Competing financial interests: The authors declare no competing financial interests.

How to cite this article: Pannuzzo, M., Raudino, A., Milardi, D., La Rosa, C. & Karttunen, M. α -Helical Structures Drive Early Stages of Self-Assembly of Amyloidogenic Amyloid Polypeptide Aggregate Formation in Membranes. *Sci. Rep.* **3**, 2781; DOI:10.1038/srep02781 (2013).



This work is licensed under a Creative Commons Attribution-NonCommercial-ShareAlike 3.0 Unported license. To view a copy of this license, visit <http://creativecommons.org/licenses/by-nc-sa/3.0>